Research Article | Vol. 28, No. 23 / 9 November 2020 / Optics Express 34960
Optics EXPRESS

Structural and optical properties of monocrystalline and polycrystalline gold plasmonic nanorods

LUKÁŠ KEJÍK,[1,3,*] MICHAL HORÁK,[1,3] TOMÁŠ ŠIKOLA,[1,2] AND VLASTIMIL KŘÁPEK[1,2]

[1]Central European Institute of Technology, Brno University of Technology, Purkyňova 123, 612 00 Brno, Czech Republic
[2]Institute of Physical Engineering, Brno University of Technology, Technická 2, 616 69 Brno, Czech Republic
[3]These authors contributed equally
[*]lukas.kejik@ceitec.vutbr.cz

Abstract: The quality of lithographically prepared structures is intimately related to the properties of the metal film from which they are fabricated. Here we compare two kinds of thin gold films on a silicon nitride membrane: a conventional polycrystalline thin film deposited by magnetron sputtering and monocrystalline gold microplates that were chemically synthesised directly on the membrane's surface for the first time. Both pristine metals were used to fabricate plasmonic nanorods using focused ion beam lithography. The structural and optical properties of the nanorods were characterized by analytical transmission electron microscopy including electron energy loss spectroscopy. The dimensions of the nanorods in both substrates reproduced well the designed size of 240×80 nm^2 with the deviations up to 20 nm in both length and width. The shape reproducibility was considerably improved among monocrystalline nanorods fabricated from the same microplate. Interestingly, monocrystalline nanorods featured inclined boundaries while the boundaries of the polycrystalline nanorods were upright. Q factors and peak loss probabilities of the modes in both structures are within the experimental uncertainty identical. We demonstrate that the optical response of the plasmonic nanorods is not deteriorated when the polycrystalline metal is used instead of the monocrystalline metal.

1. Introduction

Plasmonic antennas are metallic particles widely studied for their ability to control, enhance, and concentrate electromagnetic field [1]. Strikingly, the field in the vicinity of plasmonic antennas, the so-called near field, can be focused into a deeply subwavelength region [2]. At the same time, the field is strongly enhanced with respect to the driving field, which can be e.g. a plane wave. Focusing of the field stems from the excitation of localized surface plasmons (LSP) – quantized oscillations of the free electron gas in the metal coupled to the evanescent electromagnetic wave propagating along the boundary of the metal. Thanks to this light-concentrating ability, plasmonic antennas have found applications in energy harvesting [3], construction of metasurfaces [4,5], luminescence enhancement [6], or biodetection [7].

Plasmonic antennas are conventionally prepared using electron beam lithography, which utilizes a mask fabricated in an electron-sensitive polymer (resist), or more straightforwardly using direct milling by focused ion beam (FIB) [8]. The energy of antenna's plasmon resonance is highly dependent on the choice of antenna material and its quality, surrounding material, as well as antenna size and shape [9].

#409428 https://doi.org/10.1364/OE.409428
Journal © 2020 Received 4 Sep 2020; revised 30 Sep 2020; accepted 1 Oct 2020; published 3 Nov 2020

Optics EXPRESS

Typical plasmonic antennas fabricated from metallic layers deposited by sputtering or evaporation techniques are polycrystalline by nature with randomly oriented grains of varying sizes [10–12]. The fabrication resolution and overall shape of the antenna are then significantly affected by the size of grains present in the antenna [13] making each antenna of a slightly different shape. The deviations in shape or the orientation of the antennas might then be detrimental e.g. for the performance of metasurfaces as they introduce random noise into their phase response. Although by optimizing the deposition parameters, the resulting grain size can be somewhat tuned [14], the presence of grain boundaries within an antenna is related to the lower resonance quality factor and higher relaxation rates [15]. These detrimental effects can be considerably reduced by a subsequent annealing [16,17]. In combination with other approaches, like template stripping, the layer quality might be improved even further [18], and increased grain size can then allow antenna fabrication from a single grain. This can be achieved readily by chemical synthesis where each particle can be made as single crystal grain with great shape variability [19] which should provide the optimum optical properties [20], but their precise placement on the substrate is hard to achieve. In an ideal case, the whole set of antennas is fabricated from a single grain, possibly large metallic 2D monocrystal [21,22] placed on a supporting substrate, alleviating the troubles with the size and shape reproducibility in the follow-up lithographic process. In the case of gold, there are several approaches to chemically reduce typically $HAuCl_4$ into large monocrystalline microplates in pathways based on aniline [23], two-component ionic liquids [24], ethylene glycol [25–27] or tetraoctylammonium bromide (TOABr) [28–30] where the latter two are the most prevalent. Although the improvement in optical properties of monocrystalline versus polycrystalline gold is not that radical in bulk [31], it has been shown as a useful platform with improved propagation length of surface plasmons [32] even in complex devices [33–36]. Additionally, in terms of fabrication of antennas or more complex structures, monocrystalline gold allows fabrication with higher resolution, generally better-defined shape, and consequently better optical performance [37,38].

A detailed study, though, comparing the polycrystalline and monocrystalline antennas in terms of material properties and correlating the antenna shape with plasmon modes with high spatial and energy resolution, has been missing in the literature.

Here we show a direct comparison of gold plasmonic nanorods fabricated either from monocrystalline or polycrystalline gold substrates using FIB lithography. We selected the nanorod shape due to well-isolated modes and the existence of analytical description [39]. We characterize the material properties of the input substrates as well as the resulting nanorods, correlate the nanorod shape with its plasmonic properties and visualize the supported plasmonic modes by scanning transmission electron microscopy (STEM) in combination with electron energy loss spectroscopy (EELS) with nanometer spatial resolution not achievable by means of other methods.

2. Methods

2.1. Fabrication of nanorod antennas

Both nanorod fabrication routes are schematically displayed in Supplement 1, Fig. S1. Gold monocrystalline microplates, grown directly on the surface of the membranes used in transmission electron microscopy (TEM), were prepared using the modified procedure by Radha and Kulkarni [29]. Briefly, 4 ml of TOABr solution in toluene (50 mM) was stirred vigorously while 1.6 ml of aqueous $HAuCl_4$ (25 mM) was injected. The resulting mixture of two immiscible phases, aqueous and toluene-based, was stirred for approximately 2 minutes. The aqueous component then became colourless while the toluene component became red-coloured which is related to the phase transfer of $(AuCl_4)^-$ ions from aqueous solution into toluene using TOABr as a phase transfer agent. Toluene solution containing $(AuCl_4)^-$ – TOABr precursor was then extracted and 1–2 µl were typically applied onto the SiN_x TEM membrane (Agar Scientific), which was Kapton-taped

Optics EXPRESS

to a piece of silicon wafer for easier manipulation, on a preheated hot plate (75 °C). When toluene evaporated, the temperature was set to 140 or 145 °C held for 35–45 hours. Such procedure resulted in monocrystalline gold microplates of various lateral sizes (tens of micrometers) and thickness (tens to hundreds of nanometers) and the remaining precursor residues were washed away in toluene, ethanol, and water baths, respectively. Note that the thinnest microplates (below 100 nm) were pre-selected using bright field optical microscopy due to their partial transparency resulting in the pink shade as opposed to thicker ones which reflected the light completely (see Supplement 1, Fig. S2). The final information about the thickness was obtained using EELS.

The polycrystalline gold layer (thickness of 30 nm) was deposited by magnetron sputtering using Leica coater EM ACE600 directly (i.e. with no adhesion layer) on a 30-nm-thick SiN_x membrane.

Gold nanorods on both samples were fabricated by FIB lithography in dual-beam FIB/SEM microscope FEI Helios using gallium ions with the energy of 30 keV and ion beam current of 1.3 pA. Note that the energy (the highest available) and the current (the lowest available) are optimized for the best spatial resolution of the milling [8]. The nanorods were designed as rectangles with the length of 240 nm and the width of 80 nm. They were situated in the middle of a $1.5 \times 1\ \mu m^2$ metal-free rectangle, which is perfectly sufficient to prevent their interaction with the surrounding metallic layer. Note that the amount of residual gallium ions is negligible and does not influence the localized surface plasmon resonances [8]. Results of the energy-dispersive X-ray spectroscopy (EDS) analysis are shown in Supplement 1, Fig. S3. We note that we have experienced some effect of anisotropic sputtering efficiency of the FIB [40] which resulted in inclined boundaries of monocrystalline nanorods as detailed in Section 3.

Finally, we remark that we have experienced issues with the mechanical stability of the membranes with monocrystalline nanorods which proved to be more brittle than untreated ones. In total, we have fabricated five monocrystalline samples containing microplates of a suitable thickness (below 100 nm). Three samples have been destroyed during the fabrication process or sample manipulation and the last two were characterized in the TEM. For the latter ones, it was possible to obtain the majority of the properties, although no membrane survived complete analysis. Therefore, a complete characterization of a single sample turned out impossible and we used different samples instead. We have not experienced any stability issues for the polycrystalline substrates. We suppose that the low stability of the monocrystalline substrates is related to the membrane heating, its loading with the growth solution, or by the following washing procedure in various liquid solvents. Conversely, a continuous thin film of polycrystalline gold does not undergo any wet treatment and can even contribute to the mechanical strength of the membrane unlike the finite-size monocrystalline microplates with rather low coverage.

2.2. Analytical methods

Surface roughness of the resulting polycrystalline and monocrystalline gold substrates was analysed by atomic force microscopy (AFM) using Bruker Dimension Icon in tapping ScanAsyst mode.

Analytical transmission electron microscopy characterization including STEM-EELS was performed using TEM FEI Titan equipped with Super-X spectrometer for EDS and GIF Quantum spectrometer for EELS operated at the primary electron energy of 300 keV. Prior to STEM-EELS experiments, all samples were cleaned in oxygen/argon plasma for 10 seconds to prevent the carbon contamination [8]. Beam current was set around 0.2 nA, the full-width at half-maximum (FWHM) of the zero-loss peak (ZLP) was in the range from 0.1 eV to 0.15 eV, and the beam diameter was approximately 1 nm. We set the convergence semi-angle to 10 mrad and the collection semi-angle to 20.5 mrad. We note that these parameters are not critical for the signal-to-background ratio of the setup. Additionally, the 300 keV primary beam energy is necessary to achieve spatial maps of LSP resonances with a good signal-to-noise ratio also in

Optics EXPRESS

the pixels recorded on the gold (as the thickness of monocrystalline nanorods is up to 50 nm). We also note that the signal-to-ZLP ratio depends rather weakly on the primary beam energy [41]. The dispersion of the spectrometer was 0.01 eV/pixel. We recorded spectrum images with the pixel size of 2 nm. Every pixel consists of 1 EEL spectrum whose acquisition time was adjusted to use the maximal intensity range of the CCD camera in the spectrometer and avoid its overexposure. Immediately after recording the spectrum images, their ZLPs were aligned to compensate for a possible energy drift during the whole spectrum image acquisition. EEL spectra were integrated over rectangular areas consisting of tens of pixels in the areas corresponding to the maximum loss probability of studied LSP resonances. From the recorded spectra we have subtracted the background represented by EEL spectra integrated over rectangular areas on the clean membrane with no contribution of LSP-related signal. Obtained spectra were divided by the integral intensity of the ZLP (the energy window for integration was set as −1 eV to +1 eV) to transform measured counts to a quantity proportional to the loss probability. We fitted the peaks in the EEL spectra by Gaussian function to determine the peak energy and its spectral width (i.e., FWHM). EEL maps were calculated by dividing the map of integrated intensity at the plasmon peak energy with the energy window of 0.1 eV by the map of the integral intensity of the ZLP.

Simulations of EELS spectra have been carried out using the boundary element method (BEM) [42] with a software package MNPBEM [43]. BEM is considered as a state-of-the-art method for the simulations of EELS utilized in the majority of studies in the field, capable to treat plasmonic structures of an arbitrary shape (planar or three-dimensional), including realistic shapes retrieved by electron tomography [44]. The dielectric function of gold was taken from Ref. [45] and the dielectric constant of the silicon nitride membrane was set equal to 4, which is a reasonable approximation in the considered spectral region [46] taking into account non-stoichiometric composition of the membrane [8]. The polycrystalline nanorods have been represented by a rectangular prism and the monocrystalline nanorods by a truncated pyramid with the top face reduced by 30 nm from each side in comparison to the bottom face (i.e., with the length and width smaller by 60 nm). The edges of the nanorods have been rounded with a radius of 10 nm.

3. Structural properties of the nanorods

Thin monocrystalline microplates and polycrystalline films of gold have been characterized by selected-area electron diffraction (SAED) in TEM and by AFM. Figure 1(a) shows a monocrystalline microplate with fabricated nanorods and corresponding electron diffraction pattern recorded at an area away from the nanorods. The diffraction pattern exhibits a 6-fold rotational symmetry and corresponds to the face-centered cubic (FCC) Au crystal lattice viewed along the [111] direction. A point-like symmetric character of the pattern indicates the single-crystalline nature of the synthesized Au microplates laying flat on the membrane with (111)-oriented basal plane.

A similar characterization of a polycrystalline thin film is shown in Fig. 1(b). For the selected scale, the individual grains of the polycrystal are not well visible [see Fig. 2(b) for a zoomed-in images]. Nevertheless, a circular diffraction pattern clearly corresponds to a polycrystalline sample with a random orientation of individual grains.

AFM has been performed for a different set of pristine samples fabricated under the same growth conditions as the samples with nanorods. It reveals a rather flat surface of both monocrystalline [Fig. 1(c)] and polycrystalline [Fig. 1(d)] samples, with root mean square surface roughness on average around 0.6 nm for the monocrystalline and 1.2 nm for the polycrystalline substrates. Larger roughness of the polycrystalline film is related to a stochastic nature of the gold sputtering.

The overview of resulting nanorod shapes that underwent EELS analysis is shown in Fig. 2. Monocrystalline nanorods are rather regular, with smooth boundaries. However, the tips of the rods are faceted and deviate from the rectangular shape. The area surrounding the nanorods is clean and smooth (i.e., it shows no features in the STEM). Polycrystalline nanorods are of more

Optics EXPRESS

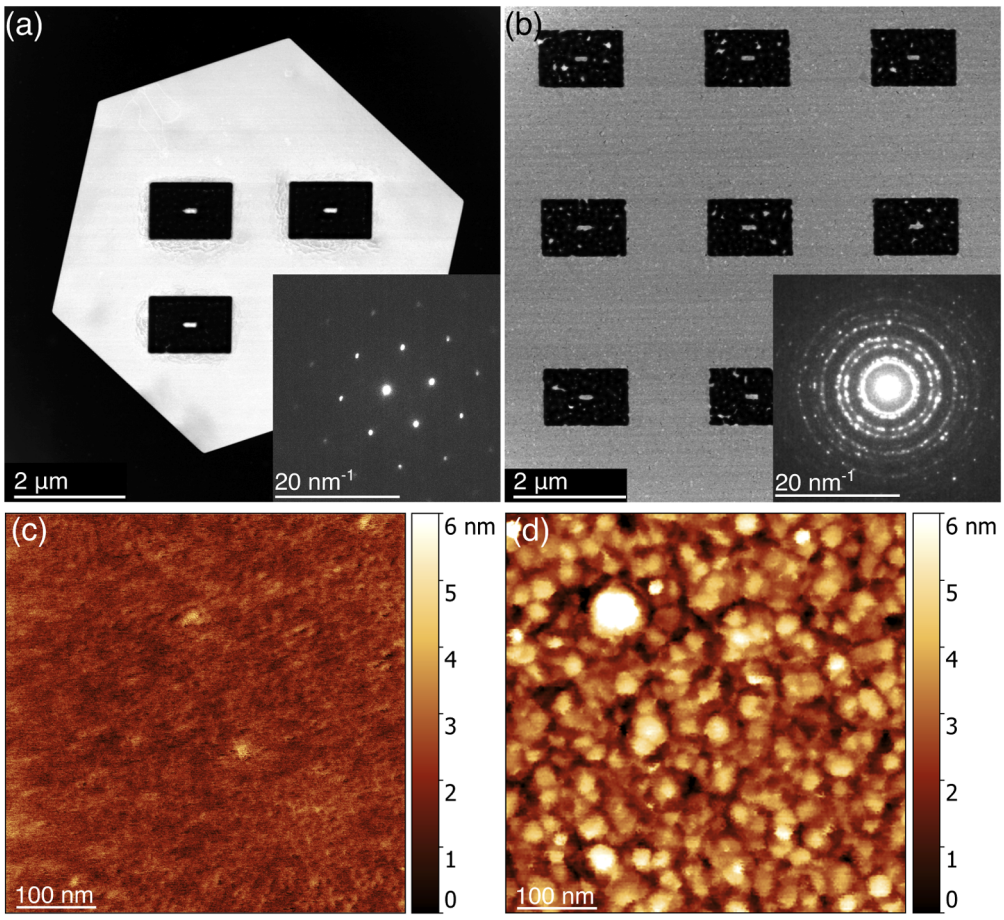

Fig. 1. (a,b) STEM ADF image of (a) a monocrystalline microplate and (b) a polycrystalline thin film after the fabrication of nanorods. Insets show electron diffraction patterns recorded in the area of the film far from the nanorods. (c,d) AFM images of the surface of a typical (c) monocrystalline microplate and (d) a polycrystalline thin film.

irregular shape, with coarse boundaries and overall larger deviations from the desired rectangular shape. The irregularity and larger variance are related to the random orientation of grains in the polycrystalline metal layer, for which different sputtering efficiencies apply during the FIB lithography [40]. Individual grains of gold are visible in the STEM images, with typical sizes between 20 and 50 nm. Nevertheless, polycrystalline nanorods lack the faceted tips and some may reproduce the desired rectangular shape better than monocrystalline nanorods [e.g. 1^{st} and 2^{nd} rod in Fig. 2(b)]. The area around the polycrystalline nanorods is covered by gold crystallites due to incomplete removal of the gold layer again related to the different milling efficiency of randomly orientated gold grains. We note that it is not possible to remove these crystallites simply by increasing the removal time as it would result in thinning and finally a destruction of the membrane underneath. Upon close inspection, monocrystalline nanorods fabricated from the same gold monocrystal exhibit very similar overall shape with the tips faceted in the same manner which is also reflected in much smaller deviations in terms of e.g. nanorod length (Table 1). Across the different microplates though the facets look very different. When comparing the respective orientation of gold monocrystal and the resulting nanorods, some of the monocrystal's side facets seem to be imprinted into the nanorod shape (see Supplement 1, Fig. S4). Therefore,

Optics EXPRESS

the fabrication results might be further improved by a suitable alignment of the monocrystal side facets with the FIB milling direction.

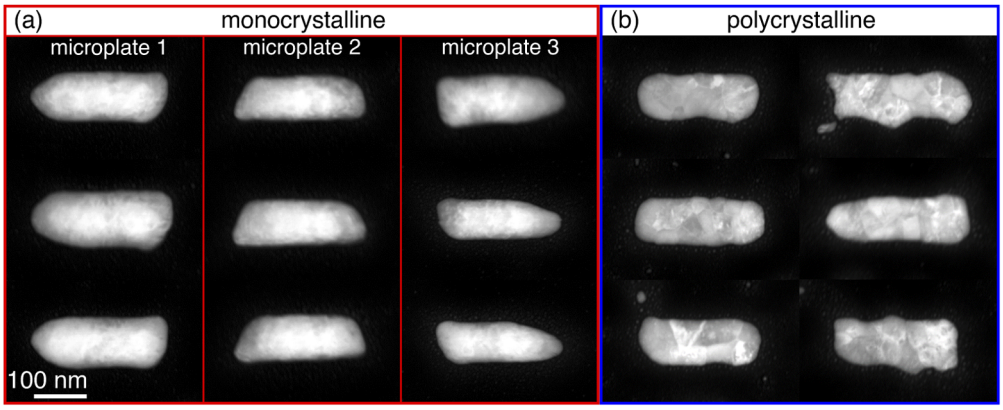

Fig. 2. STEM ADF images of gold nanorods fabricated from (a) monocrystalline and (b) polycrystalline gold substrates. Note that monocrystalline nanorods are divided into columns according to the microplate from which they were fabricated.

Table 1. Summary of average dimensions and plasmon resonance parameters of polycrystalline and monocrystalline gold nanorods characterized by EELS followed by parameters averaged only over nanorods originating from the same gold monocrystalline microplate. Note that the numbers in parentheses in the left column correspond to the number or analysed nanorods. The values of calculated Q factors include the convolution with the Gaussian (FWHM 0.3 eV) accounting for the instrumental broadening.

	Length (nm)	Width (nm)	LD energy (eV)	LD Q factor	LQ energy (eV)	LQ Q factor
Polycrystalline - all (7)	238 ± 14	84 ± 3	1.01 ± 0.05	3.2 ± 0.4	1.67 ± 0.08	4.5 ± 0.6
Monocrystalline - all (9)	232 ± 9	82 ± 7	1.14 ± 0.03	3.4 ± 0.3	1.78 ± 0.03	5.1 ± 0.4
microplate 1 (3)	243 ± 3	90 ± 5	1.12 ± 0.03	3.1 ± 0.2	1.81 ± 0.01	4.9 ± 0.4
microplate 2 (3)	231 ± 2	80 ± 2	1.13 ± 0.01	3.4 ± 0.1	1.75 ± 0.02	5.0 ± 0.4
microplate 3 (3)	223 ± 2	76 ± 5	1.17 ± 0.02	3.7 ± 0.2	1.77 ± 0.01	5.3 ± 0.4
Theory polycrystalline	240 ± 24	80 ± 8	1.08 ± 0.07	2.8 ± 0.2	1.88 ± 0.08	5.5 ± 0.1
Theory monocrystalline	240 ± 24	80 ± 8	1.06 ± 0.08	2.9 ± 0.2	1.62 ± 0.07	4.4 ± 0.5

Representative nanorods with the targeted length and width of $240 \times 80\,\mathrm{nm}^2$ are shown in Figs. 3(a) and (c) with the corresponding thickness profiles along their length and width in Figs. 3(b) and (d). We have used EELS to retrieve the thickness of the nanorods using the same approach described in Ref. [8] based on Refs. [47–49]. Polycrystalline nanorods exhibit upright boundaries with a steep change in the thickness from zero to maximum over a distance of about 10 nm related to the diameter of the ion beam whose nominal FWHM is around 3 nm. On the other hand, monocrystalline nanorods have strongly inclined boundaries mostly due to the microplate's anisotropy with possible gold redeposition [40].

The dimensions of all the nanorods have been determined as the maximum extent of the white contrast in the STEM annular dark field (ADF) images along the longitudinal (length L) and transverse (width W) direction, and the height H has been determined as the average height of the central part of the nanorod. The dimensions of the monocrystalline nanorods were $L = (232 \pm 9)\,\mathrm{nm}$, $W = (82 \pm 7)\,\mathrm{nm}$, and $H = (52 \pm 5)\,\mathrm{nm}$, while the dimensions of the polycrystalline nanorods were $L = (238 \pm 14)\,\mathrm{nm}$, $W = (84 \pm 3)\,\mathrm{nm}$, and $H = (30 \pm 3)\,\mathrm{nm}$ (see

Optics EXPRESS

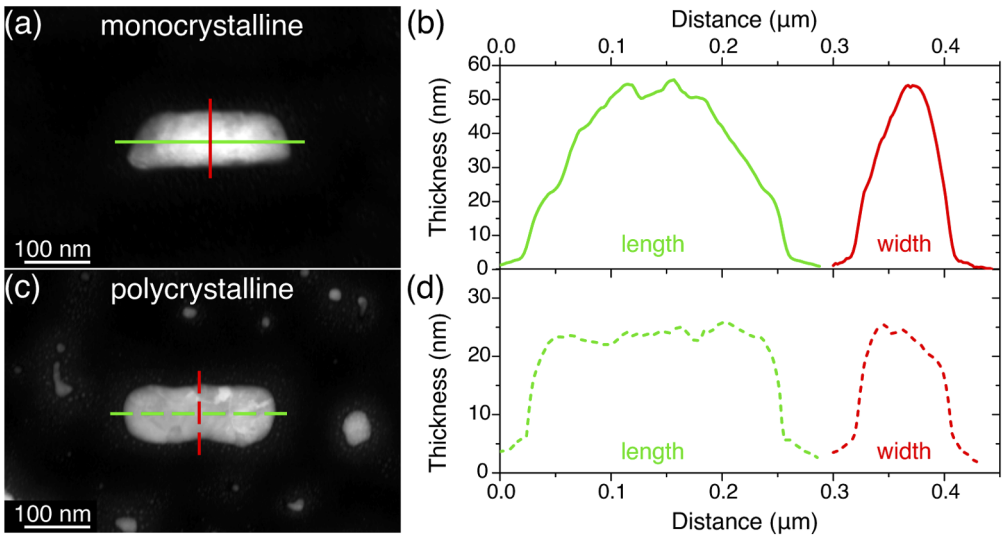

Fig. 3. (a,c) STEM ADF images of representative plasmonic nanorods fabricated from (a) a monocrystalline microplate and (c) a polycrystalline thin film with cross-sections corresponding to (b,d) thickness profiles along the long and short axes of (b) the monocrystalline and (d) polycrystalline nanorod determined by EELS. The color of the thickness profile curve corresponds to the color of the axis indicated in (a,c).

Table 1 for a complete summary). The targeted lateral dimensions have been reproduced well. The height of the monocrystalline microplates cannot be quantitatively controlled and due to the low mechanical stability of the monocrystalline samples, we measured the height only after the fabrication of the nanorods together with the EELS characterization of plasmon modes. We could fabricate the polycrystalline nanorods (for which the height is controlled rather accurately) after the characterization of the monocrystalline nanorods, assuring the same thickness. However, this would necessarily result in some deviation in the alignment and adjustment of the electron microscopes used for the fabrication of the nanorods and their characterization, restricting the comparability of both types of nanorods. Therefore, we preferred the fabrication and characterization of both samples without any delay and need for realignment of the microscopes at the price of different nanorod heights. In addition, the inclined boundaries of the monocrystalline nanorods resulted in the LSP energies nearly the same as for the polycrystalline nanorods, which is optimum for the comparison of both systems despite their different height.

4. Optical properties of the nanorods

Two red and blue curves in Fig. 4 represent typical experimental loss probability spectra of two monocrystalline and two polycrystalline nanorods. The lowest-order LSP mode is observed around 1.1 eV and by inspecting energy-filtered maps of the loss intensity in Figs. 5(a) and (c), it is identified as the longitudinal dipole (LD) mode. The peak at 1.8 eV is attributed to two spectrally overlapping modes, the longitudinal quadrupole (LQ) mode, and the transverse dipole (TD) mode. It is difficult to resolve the LQ and TD modes in the experiment, as well as the higher-order modes. Nevertheless, the energy-filtered maps of the loss intensity for the peak energy [Figs. 5(b) and (d)] suggest LQ mode to be dominant at the peak energy.

Both main peaks of the experimental spectra corresponding to monocrystalline nanorods are slightly blue-shifted with respect to polycrystalline ones. Since the differences in the dielectric function of monocrystalline and polycrystalline gold have been previously found as insignificant

Optics EXPRESS

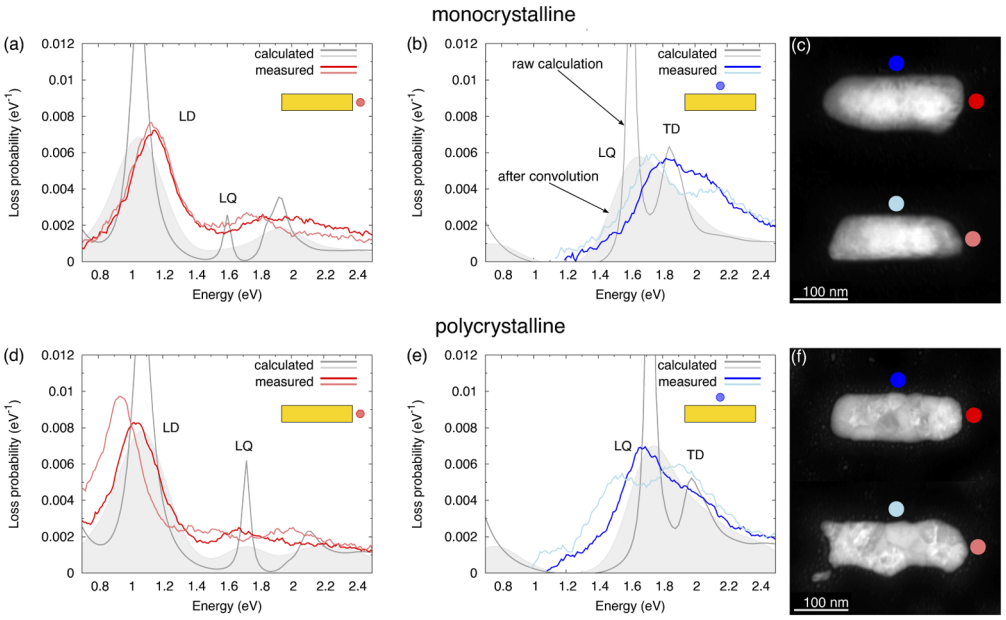

Fig. 4. Loss probability spectra for (a,b) monocrystalline and (d,e) polycrystalline nanorods recorded for the electron beam located at (a,d) the center of the short edge and (b,e) the center of the long edge for two different (c) monocrystalline and (f) polycrystalline nanorods. Experimental spectra are displayed by red or blue lines. Calculated spectra are displayed by gray lines, calculated spectra broadened by a Gaussian with 0.3 eV FWHM to reproduce the instrumental broadening are displayed by the gray shaded area. Most significant LSP modes are labelled as LD (longitudinal dipole), LQ (longitudinal quadrupole), and TD (transverse dipole) mode. (c,f) STEM ADF images of the selected nanorods with color spots indicating the position of the electron beam with colors corresponding to the respective EEL spectra.

[31], we attribute the blue shift to the differences in the shape and thickness of the nanorods. The experimental loss probability spectra are accompanied by those calculated using MNPBEM shown as grey lines. The simulations take into account actual height profiles of the nanorods as determined by EELS, i.e., the height of 50 nm with inclined boundaries for the monocrystalline nanorods and the height of 30 nm with upright boundaries for the polycrystalline nanorods. Note that the larger thickness causes a shift towards higher mode energies while the presence of inclined boundaries causes a shift to lower energies, as shown in Supplement 1, Fig. S5. To account for the experimental spectral broadening of our EELS system, the simulated spectra were convoluted with a Gaussian of 0.3 eV FWHM shown as shaded gray spectra. These broadened spectra are then in good agreement with the experimental ones.

By fitting the spectral profile of the modes by a Gaussian, we obtained the LSP resonance energy E, and Q factor, defined as the LSP resonance energy divided by FWHM, for both main modes. Mean energies of the LD mode in the experiment averaged to (1.14 ± 0.03) eV for the monocrystalline nanorods and (1.02 ± 0.05) eV for the polycrystalline nanorods. Taking into account the experimental resolution of EELS, estimated as 0.1 eV for our setup, no significant difference in the energy of LD mode has been observed between monocrystalline and polycrystalline nanorods. The simulations accounting for the dispersion in length and width of nanorods [10 % deviations from the mean value are assumed, i.e., L = (240 ± 24) nm, W = (80 ± 8) nm] yielded the energies of the LD mode in the range (1.06 ± 0.08) eV for monocrystalline and (1.08 ± 0.07) eV for polycrystalline nanorods, in good agreement with the

Optics EXPRESS

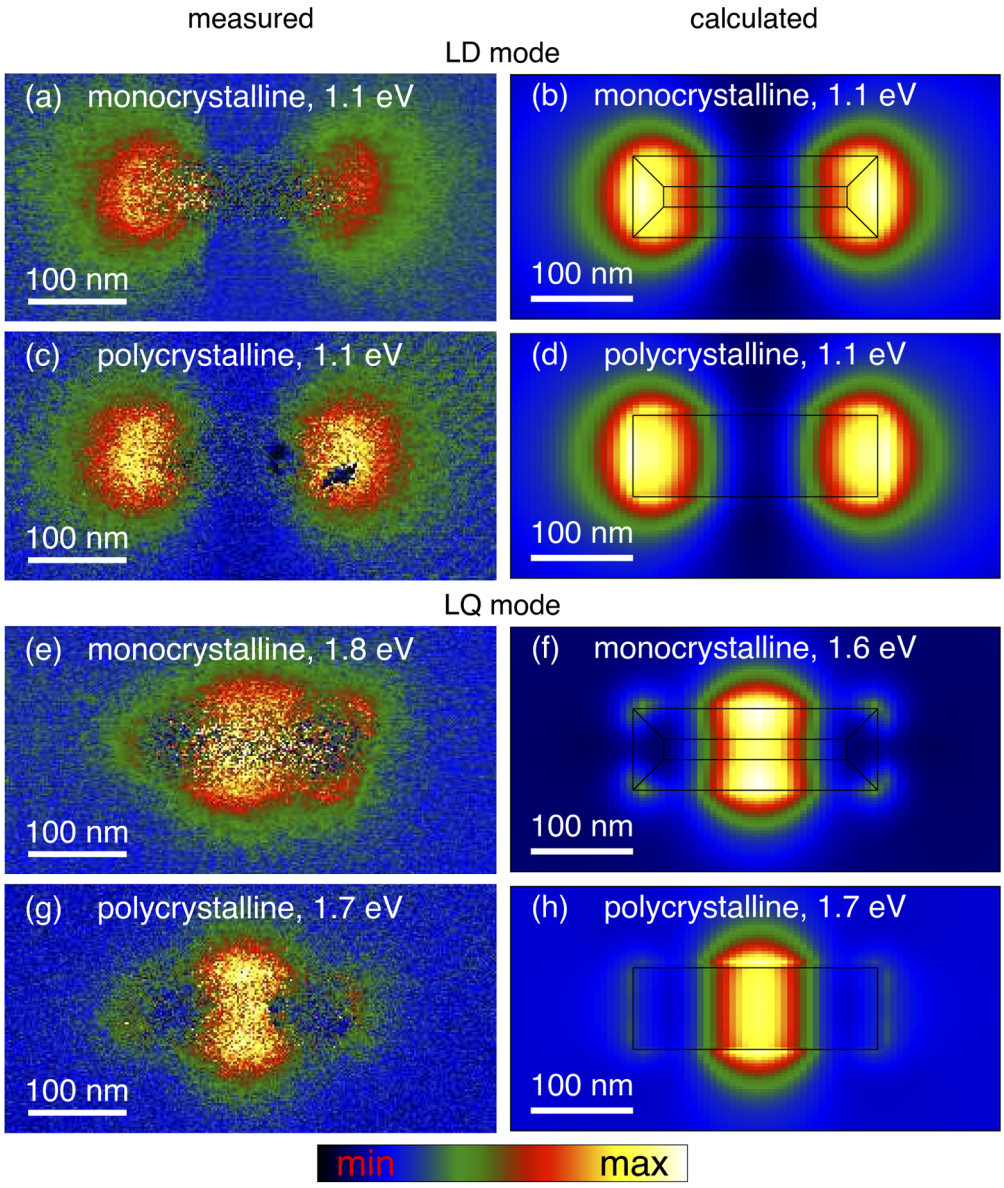

Fig. 5. Spatial distribution of the loss probability at the energy of (a-d) the LD mode and (e-h) the LQ mode. Left panels (a,c,e,g) show experimental maps for nanorods displayed in the upper part of Figs. 4(c) and (f). Right panels (b,d,f,h) show calculated values with the contour of the nanorod displayed by the black lines. The energy of the mode is indicated at the top part of each panel. The color scale at the bottom is common to all panels.

Optics EXPRESS

experimental values taking into account the experimental error and uncertainty of the shape and dimensions of model nanorods.

The values of Q factors of the LD mode determined from the experiment correspond to 3.4 ± 0.3 for monocrystalline nanorods and 3.2 ± 0.4 for polycrystalline nanorods. The raw calculated values of Q factors of the LD mode correspond to 8.4 ± 0.3 for monocrystalline nanorods and 7.5 ± 0.3 for polycrystalline nanorods. Naturally, these values are not directly comparable to the experimental ones that are influenced by the instrumental broadening. After convolving the calculated spectra with the Gaussian (FWHM 0.3 eV) the Q factors are reduced to 2.9 ± 0.2 for monocrystalline nanorods and 2.8 ± 0.3 for polycrystalline nanorods, being now in good agreement with the experimental values. The differences between the monocrystalline and polycrystalline nanorods are again insignificant.

To confirm the nature of the LSP modes induced in gold nanorods, we extracted EEL maps to visualize the modes at the peak energies. Figures 5(a) and (c) show EEL maps at the 1.1 eV energy for monocrystalline and polycrystalline gold nanorods with a loss probability distribution typical for the LD mode. Similarly, the EEL maps at a higher energy peak at 1.8 eV for monocrystalline and 1.7 eV for polycrystalline nanorods [Figs. 5(e) and (g)] imply that the longitudinal quadrupole mode is more prevalent than the transverse dipole mode at the peak energy. EEL maps for both modes show only minute differences between monocrystalline and polycrystalline nanorod, although the modes in polycrystalline one can be resolved a bit easier. For a detailed interpretation of the EEL maps, we refer to Ref. [50]. The experimental EEL maps were complemented by the simulated EEL maps with a very good agreement in both LD [Figs. 5(b) and (d)] and LQ [Figs. 5(f) and (h)] mode after taking into account the differences in the nanorod morphology.

Table 1 summarizes the morphological as well as optical properties of all studied nanorods. In total, we have analysed 7 polycrystalline and 9 monocrystalline nanorods which were fabricated using in total three monocrystalline microplates. In terms of the nanorods' size the average length of the polycrystalline nanorods was closer to the desired length (240 nm) though with larger deviations, the width of the monocrystalline nanorods was closer to the desired width (80 nm) also with larger deviations. The average energy of LD mode for the monocrystalline nanorods is slightly larger and with smaller overall dispersion than for polycrystalline ones, the difference is even more pronounced in the case of LQ mode. Similarly, the extracted Q factors are slightly larger in the case of monocrystalline nanorods for both modes. Overall the average parameters of the nanorods' plasmon resonance for monocrystalline and polycrystalline nanorods are quite similar. Although when we focus on the nanorods fabricated from within the same gold microplate, the dispersion of measured parameters is significantly reduced, especially in terms of LD and LQ mode energy.

While we have found insignificant differences between the optical properties of monocrystalline and polycrystalline plasmonic structures, some previous works report better performance of monocrystalline structures or structures with larger grains. We will now explain that their results are not contradictory to ours. One of the previous studies reported stark differences between the polycrystalline and monocrystalline plasmonic structures in terms of optical scattering [20]. However, the poor optical scattering of polycrystalline structures can be attributed to the presence of the chromium adhesion layer under the polycrystalline structures which strongly contributes to their plasmonic damping [51]. A considerable improvement of the optical response of the polycrystalline structures has been reported after thermal annealing [17]. However, this can be attributed to the original small size of the grains prior to annealing related to the large boundary scattering. In our case, the gold is deposited on a flat surface and the deposition procedure was optimized to obtain large grains. Therefore, our as-grown grains already have the size of the post-annealed grains of the referred study and we do not expect considerable improvement by this procedure.

Optics EXPRESS

5. Conclusions

We have prepared monocrystalline and polycrystalline plasmonic nanorods and compared their structural and optical properties. Most pronounced differences have been identified regarding the vertical interfaces of nanorods, inclined for the monocrystalline nanorods but upright for polycrystalline ones. Monocrystalline nanorods outperform the polycrystalline ones in terms of slightly reduced size and shape fluctuations. They also benefit from clean metal-free parts, while for polycrystalline nanorods these parts contain metal crystallites due to incomplete metal removal. On the other hand, monocrystalline nanorods systematically deviate from the desired shape due to preferable termination with specific crystal planes. The membranes with monocrystalline nanorods also suffered from increased brittleness.

As for the optical properties, we have observed no significant differences for both crystallinities. The plasmon resonance energies, Q factors, and loss probability magnitudes detected by EELS show no difference up to experimental accuracy. The optical response of nanorods is not deteriorated when the polycrystalline metal replaces the monocrystalline metal. To conclude, polycrystalline plasmonic antennas represent a fully-fledged alternative of monocrystalline antennas.

Funding

Ministerstvo Školství, Mládeže a Tělovýchovy (LM2018110, LQ1601); Grantová Agentura České Republiky (19-06621S).

Acknowledgments

M. H. acknowledges the support of Thermo Fisher Scientific and CSMS scholarship 2019.

Disclosures

The authors declare no conflicts of interest.

See Supplement 1 for supporting content.

References

1. L. Novotny and N. van Hulst, "Antennas for light," Nat. Photonics **5**(2), 83–90 (2011).
2. J. A. Schuller, E. S. Barnard, W. Cai, Y. C. Jun, J. S. White, and M. L. Brongersma, "Plasmonics for extreme light concentration and manipulation," Nat. Mater. **9**(3), 193–204 (2010).
3. C. F. Guo, T. Sun, F. Cao, Q. Liu, and Z. Ren, "Metallic nanostructures for light trapping in energy-harvesting devices," Light: Sci. Appl. **3**(4), e161 (2014).
4. J. Babocký, A. Křížová, L. Štrbková, L. Kejík, F. Ligmajer, M. Hrtoň, P. Dvořák, M. Týč, J. Čolláková, V. Křápek, R. Kalousek, R. Chmelík, and T. Šikola, "Quantitative 3D phase imaging of plasmonic metasurfaces," ACS Photonics **4**(6), 1389–1397 (2017).
5. A. Faßbender, J. Babocký, P. Dvorák, V. Krápek, and S. Linden, "Direct phase mapping of broadband laguerre-gaussian metasurfaces," APL Photonics **3**(11), 110803 (2018).
6. S. Butun, S. Tongay, and K. Aydin, "Enhanced light emission from large-area monolayer mos2 using plasmonic nanodisc arrays," Nano Lett. **15**(4), 2700–2704 (2015).
7. J. R. Mejía-Salazar and O. N. Oliveira, "Plasmonic biosensing," Chem. Rev. **118**(20), 10617–10625 (2018).
8. M. Horák, K. Bukvišová, V. Švarc, J. Jaskowiec, V. Křápek, and T. Šikola, "Comparative study of plasmonic antennas fabricated by electron beam and focused ion beam lithography," Sci. Rep. **8**(1), 9640 (2018).
9. K. L. Kelly, E. Coronado, L. L. Zhao, and G. C. Schatz, "The optical properties of metal nanoparticles: The influence of size, shape, and dielectric environment," J. Phys. Chem. B **107**(3), 668–677 (2003).
10. S. Kobayashi, H. Takagi, and T. Watanabe, "Grain boundary character distribution and texture evolution during surface energy-driven grain growth in nanocrystalline gold thin films," Philos. Mag. **93**(10-12), 1425–1442 (2013).
11. N. Hiramatsu, F. Kusa, K. Imasaka, I. Morichika, A. Takegami, and S. Ashihara, "Propagation length of mid-infrared surface plasmon polaritons on gold: Impact of morphology change by thermal annealing," J. Appl. Phys. **120**(17), 173103 (2016).

Optics EXPRESS

12. P. Parajuli, R. Mendoza-Cruz, U. Santiago, A. Ponce, and M. J. Yacamán, "The evolution of growth, crystal orientation, and grain boundaries disorientation distribution in gold thin films," Cryst. Res. Technol. **53**(8), 1800038 (2018).
13. J. S. Huang, V. Callegari, P. Geisler, C. Brüning, J. Kern, J. C. Prangsma, X. Wu, T. Feichtner, J. Ziegler, P. Weinmann, M. Kamp, A. Forchel, P. Biagioni, U. Sennhauser, and B. Hecht, "Atomically flat single-crystalline gold nanostructures for plasmonic nanocircuitry," Nat. Commun. **1**(1), 150 (2010).
14. N. Mahmoodi, A. I. Rushdi, J. Bowen, A. Sabour, C. Anthony, P. M. Mendes, J. A. Preece, N. Mahmoodi, A. Ibrahim, R. Rushdi, J. Bowen, A. Sabouri, and C. J. Anthony, "Room temperature thermally evaporated thin Au film on Si suitable for application of thiol self-assembled monolayers in mems/nems sensors," J. Vac. Sci. Technol., A **35**(4), 041514 (2017).
15. W. Huang, W. Qian, M. A. El-Sayed, Y. Ding, and Z. L. Wang, "Effect of the lattice crystallinity on the electron-phonon relaxation rates in gold nanoparticles," J. Phys. Chem. C **111**(29), 10751–10757 (2007).
16. K. P. Chen, V. P. Drachev, J. D. Borneman, A. V. Kildishev, and V. M. Shalaev, "Drude relaxation rate in grained gold nanoantennas," Nano Lett. **10**(3), 916–922 (2010).
17. M. Bosman, L. Zhang, H. Duan, S. F. Tan, C. A. Nijhuis, C. W. Qiu, and J. K. Yang, "Encapsulated annealing: Enhancing the plasmon quality factor in lithographically-defined nanostructures," Sci. Rep. **4**(1), 5537 (2015).
18. K. M. McPeak, S. V. Jayanti, S. J. Kress, S. Meyer, S. Iotti, A. Rossinelli, and D. J. Norris, "Plasmonic films can easily be better: Rules and recipes," ACS Photonics **2**(3), 326–333 (2015).
19. M. R. Langille, M. L. Personick, J. Zhang, and C. A. Mirkin, "Defining rules for the shape evolution of gold nanoparticles," J. Am. Chem. Soc. **134**(35), 14542–14554 (2012).
20. L. Shao, Y. Tao, Q. Ruan, J. Wang, and H. Q. Lin, "Comparison of the plasmonic performances between lithographically fabricated and chemically grown gold nanorods," Phys. Chem. Chem. Phys. **17**(16), 10861–10870 (2015).
21. H. Hu, J. Zhou, Q. Kong, and C. Li, "Two-dimensional Au nanocrystals: Shape/size controlling synthesis, morphologies, and applications," Part. Part. Syst. Charact. **32**(8), 796–808 (2015).
22. Y. Chen, Z. Fan, Z. Zhang, W. Niu, C. Li, N. Yang, B. Chen, and H. Zhang, "Two-dimensional metal nanomaterials: synthesis, properties, and applications," Chem. Rev. **118**(13), 6409–6455 (2018).
23. Z. Guo, Y. Zhang, Y. DuanMu, L. Xu, S. Xie, and N. Gu, "Facile synthesis of micrometer-sized gold nanoplates through an aniline-assisted route in ethylene glycol solution," Colloids Surf., A **278**(1-3), 33–38 (2006).
24. H. Kawasaki, T. Yonezawa, K. Nishimura, and R. Arakawa, "Fabrication of submillimeter-sized gold plates from thermal decomposition of HAuCl4 in two-component ionic liquids," Chem. Lett. **36**(8), 1038–1039 (2007).
25. X. Wu, R. Kullock, E. Krauss, and B. Hecht, "Single-crystalline gold microplates grown on substrates by solution-phase synthesis," Cryst. Res. Technol. **50**(8), 595–602 (2015).
26. E. Krauss, R. Kullock, X. Wu, P. Geisler, N. Lundt, M. Kamp, and B. Hecht, "Controlled growth of high-aspect-ratio single-crystalline gold platelets," Cryst. Growth Des. **18**(3), 1297–1302 (2018).
27. K. J. Kaltenecker, E. Krauss, L. Casses, M. Geisler, B. Hecht, N. A. Mortensen, P. U. Jepsen, and N. Stenger, "Mono-crystalline gold platelets: a high-quality platform for surface plasmon polaritons," Nanophotonics **9**(2), 509–522 (2020).
28. B. Radha, M. Arif, R. Datta, T. K. Kundu, and G. U. Kulkarni, "Movable Au microplates as fluorescence enhancing substrates for live cells," Nano Res. **3**(10), 738–747 (2010).
29. B. Radha and G. U. Kulkarni, "A real time microscopy study of the growth of giant Au microplates," Cryst. Growth Des. **11**(1), 320–327 (2011).
30. B. Radha and G. U. Kulkarni, "Giant single crystalline Au microplates," Curr. Sci. **102**, 70–77 (2012).
31. R. L. Olmon, B. Slovick, T. W. Johnson, D. Shelton, S.-H. Oh, G. D. Boreman, and M. B. Raschke, "Optical dielectric function of gold," Phys. Rev. B **86**(23), 235147 (2012).
32. M. Prämassing, M. Liebtrau, H. J. Schill, S. Irsen, and S. Linden, "Interferometric near-field characterization of plasmonic slot waveguides in single-and poly-crystalline gold films," Opt. Express **28**(9), 12998 (2020).
33. K. M. See, F. C. Lin, and J. S. Huang, "Design and characterization of a plasmonic doppler grating for azimuthal angle-resolved surface plasmon resonances," Nanoscale **9**(30), 10811–10819 (2017).
34. B. Frank, P. Kahl, D. Podbiel, G. Spektor, M. Orenstein, L. Fu, T. Weiss, M. H. V. Hoegen, T. J. Davis, F. J. Z. Heringdorf, and H. Giessen, "Short-range surface plasmonics: Localized electron emission dynamics from a 60-nm spot on an atomically flat single-crystalline gold surface," Sci. Adv. **3**(7), e1700721 (2017).
35. S. Boroviks, F. Todisco, N. A. Mortensen, and S. I. Bozhevolnyi, "Use of monocrystalline gold flakes for gap plasmon-based metasurfaces operating in the visible," Opt. Mater. Express **9**(11), 4209 (2019).
36. H. Siampour, O. Wang, V. A. Zenin, S. Boroviks, P. Siyushev, Y. Yang, V. A. Davydov, L. F. Kulikova, V. N. Agafonov, A. Kubanek, N. A. Mortensen, F. Jelezko, and S. I. Bozhevolnyi, "Ultrabright single-photon emission from germanium-vacancy zero-phonon lines: deterministic emitter-waveguide interfacing at plasmonic hot spots," Nanophotonics **9**(4), 953–962 (2020).
37. B. Hoffmann, M. Y. Bashouti, T. Feichtner, M. Mačković, C. Dieker, A. M. Salaheldin, P. Richter, O. D. Gordan, D. R. Zahn, E. Spiecker, and S. Christiansen, "New insights into colloidal gold flakes: Structural investigation, micro-ellipsometry and thinning procedure towards ultrathin monocrystalline layers," Nanoscale **8**(8), 4529–4536 (2016).
38. R. Méjard, A. Verdy, O. Demichel, M. Petit, L. Markey, F. Herbst, R. Chassagnon, G. Colas-des Francs, B. Cluzel, and A. Bouhelier, "Advanced engineering of single-crystal gold nanoantennas," Opt. Mater. Express **7**(4), 1157 (2017).

Optics EXPRESS

39. R. Kalousek, P. Dub, L. Brínek, and T. Šikola, "Response of plasmonic resonant nanorods: an analytical approach to optical antennas," Opt. Express **20**(16), 17916 (2012).
40. Y. Stark, R. Frömter, D. Stickler, and H. P. Oepen, "Sputter yields of single- and polycrystalline metals for application in focused ion beam technology," J. Appl. Phys. **105**(1), 013542 (2009).
41. M. Horák and T. Šikola, "Influence of experimental conditions on localized surface plasmon resonances measurement by electron energy loss spectroscopy," Ultramicroscopy **216**, 113044 (2020).
42. F. J. García de Abajo and A. Howie, "Retarded field calculation of electron energy loss in inhomogeneous dielectrics," Phys. Rev. B **65**(11), 115418 (2002).
43. J. Waxenegger, A. Trügler, and U. Hohenester, "Plasmonics simulations with the mnpbem toolbox: Consideration of substrates and layer structures," Comput. Phys. Commun. **193**, 138–150 (2015).
44. G. Haberfehlner, A. Trügler, F. P. Schmidt, A. Hörl, F. Hofer, U. Hohenester, and G. Kothleitner, "Correlated 3D nanoscale mapping and simulation of coupled plasmonic nanoparticles," Nano Lett. **15**(11), 7726–7730 (2015).
45. P. B. Johnson and R. W. Christy, "Optical constants of the noble metals," Phys. Rev. B **6**(12), 4370–4379 (1972).
46. F. P. Schmidt, H. Ditlbacher, F. Hofer, J. R. Krenn, and U. Hohenester, "Morphing a plasmonic nanodisk into a nanotriangle," Nano Lett. **14**(8), 4810–4815 (2014).
47. R. F. Egerton, *Electron Energy-Loss Spectroscopy in the Electron Microscope* (Springer US, New York, 2011).
48. D. R. G. Mitchell, "Determination of mean free path for energy loss and surface oxide film thickness using convergent beam electron diffraction and thickness mapping: a case study using si and p91 steel," J. Microsc. **224**(2), 187–196 (2006).
49. K. Iakoubovskii, K. Mitsuishi, Y. Nakayama, and K. Furuya, "Thickness measurements with electron energy loss spectroscopy," Microsc. Res. Tech. **71**(8), 626–631 (2008).
50. V. Křápek, A. Konečná, M. Horák, F. Ligmajer, M. Stöger-Pollach, M. Hrtoň, J. Babocký, and T. Šikola, "Independent engineering of individual plasmon modes in plasmonic dimers with conductive and capacitive coupling," Nanophotonics **9**(3), 623–632 (2019).
51. S. J. Madsen, M. Esfandyarpour, M. L. Brongersma, and R. Sinclair, "Observing plasmon damping due to adhesion layers in gold nanostructures using electron energy loss spectroscopy," ACS Photonics **4**(2), 268–274 (2017).